

INSTITUT FRANCO-ALLEMAND DE RECHERCHES DE SAINT LOUIS  
DEUTSCH-FRANZÖSISCHES FORSCHUNGSINSTITUT SAINT LOUIS

SAINT-LOUIS (Haut-Rhin) - 5 rue du Général Cassagnou  
Tél. 03 89 69 50 00 - Télécopie 03 89 69 50 02

Adresse postale : F 68301 SAINT LOUIS CEDEX, BP 34  
Postanschrift: D 79574 WEIL AM RHEIN 1, Postfach 1260

## Numerical Simulation of the Ramac Benchmark Test

LEBLANC J.E.\*, NUSCA M.J.\*\*, WANG X.\*\*\*, SEILER F., SUGIHARA M.\*,  
FUJIWARA T.\*

\* Department of Aerospace Engineering, Nagoya University, Nagoya, Japan

\*\* Ballistics and Weapons Concepts Div., ARL, Aberdeen Proving Ground/MD, USA

\*\*\* Center for Advanced Numerical Engineering Simulations, Nanyang Technological Univ., Singapore

17th International Colloquium on the Dynamics of Explosions and Reactive Systems  
(ICDERS), Heidelberg, BRD, 25-30 July 1999

Ave de recherches  
Schwerpunkt 213

Diese Unterlagen dürfen nur an Bundeswehrdienststellen und an anderen NATO-Staaten weitergegeben werden.

PU 332/99

AQ F00-12-3914 31  
DTIG QUALITY INSPECTED 4

# REPORT DOCUMENTATION PAGE

Form Approved OMB No. 0704-0188

Public reporting burden for this collection of information is estimated to average 1 hour per response, including the time for reviewing instructions, searching existing data sources, gathering and maintaining the data needed, and completing and reviewing the collection of information. Send comments regarding this burden estimate or any other aspect of this collection of information, including suggestions for reducing this burden to Washington Headquarters Services, Directorate for Information Operations and Reports, 1215 Jefferson Davis Highway, Suite 1204, Arlington, VA 22202-4302, and to the Office of Management and Budget, Paperwork Reduction Project (0704-0188), Washington, DC 20503.

|  |  |   |   |
|--|--|---|---|
| 1. AGENCY USE ONLY (Leave blank)   | 2. REPORT DATE   | 3. REPORT TYPE AND DATES COVERED                            |   |
|  | 1999   | International Colloquium Report, 25-30 July 1999            |   |
| 4. TITLE AND SUBTITLE<br><br>Numerical Simulation of the Ramac Benchmark Test  |  |   | 5. FUNDING NUMBERS  |
| 6. AUTHOR(S)<br><br>J. E. Leblanc <sup>1</sup> , M. Jnusca <sup>2</sup> , X. Wang <sup>3</sup> , F. Seiler <sup>4</sup> , M. Sugihara <sup>1</sup> , T. Fujiwara <sup>1</sup>  |  |   |   |
| 7. PERFORMING ORGANIZATION NAME(S) AND ADDRESS(ES)   |  |   | 31  |
| 1. Department of Aerospace Engineering, Nagoya University, Chikusa-Ku, Nagoya, Japan 464-8603<br>2. Ballistics and Weapons Concepts Division, AMSRL-WM-BE, Army Research Lab, Aberdeen Proving Ground, MD 21005-5066<br>3. Center for Advanced Numerical Engineering Simulations, School of Mechanical and Production Engineering Nanyang Technological University, Singapore 639798<br>4. French-German Research Institute of Saint-Louis (ISL), 5 Rue du General Cassagnou F-68301 Saint-Louis, CEDEX, France  |  |   |   |
| 9. SPONSORING/MONITORING AGENCY NAME(S) AND ADDRESS(ES)<br><br>French-German Research Institute of Saint-Louis<br>BP 34, F 68301 Saint-Louis, France<br>Email: <a href="mailto:buck_k@isl.tn.fr">buck_k@isl.tn.fr</a>  |  |   | 10. SPONSORING/MONITORING AGENCY REPORT NUMBER<br><br>PU 332/99 |
| 11. SUPPLEMENTARY NOTES<br><br>Text in English.  |  |   |   |
| 12a. DISTRIBUTION/AVAILABILITY STATEMENT<br><br><b>DTIC Users Only.</b>  |  | 12b. DISTRIBUTION CODE                                      |   |
| ABSTRACT (Maximum 200 words)<br><br>Numerical simulations of the same ramac geometry and initial conditions by different numerical and physical models highlight the variety of solutions possible. The benchmark test was defined and announced within the community of ramac researchers. Three laboratories undertook the project. The numerical simulations include Navier-Stokes and Euler simulations with various levels of physical models and equations of state. The non-reactive part of the simulation produced similar steady state results in the three simulations. The chemically reactive part of the simulation produced widely different outcomes. The original experimental data and experimental conditions are presented. A description of each computer code and the resulting flowfield is included. A comparison between codes and results is achieved. |  |   |   |
| 14. SUBJECT TERMS<br><br>German, French, Accelerator, Benchmark, Axisymmetric flow,  |  |   | 15. NUMBER OF PAGES<br><br>6                                    |
|  |  |   | 16. PRICE CODE  |
| 17. SECURITY CLASSIFICATION OF REPORT<br><br>UNCLASSIFIED  | 18. SECURITY CLASSIFICATION OF THIS PAGE<br><br>UNCLASSIFIED | 19. SECURITY CLASSIFICATION OF ABSTRACT<br><br>UNCLASSIFIED | 20. LIMITATION OF ABSTRACT<br><br>UL                            |

NSN 7540-01-280-5500

Standard Form 298 (Rev. 2-89)  
Prescribed by ANSI Std. Z39-18  
298-102

## Numerical Simulation of the Ramac Benchmark Test

J. E. Leblanc<sup>1</sup>, M. Nusca<sup>2</sup>, X. Wang<sup>3</sup>, F. Seiler<sup>4</sup>, M. Sugihara<sup>1</sup>, and T. Fujiwara<sup>1</sup>

1. Department of Aerospace Engineering, Nagoya University,

Chikusa-ku, Nagoya, Japan 464-8603

[joseph@momo.nuae.nagoya-u.ac.jp](mailto:joseph@momo.nuae.nagoya-u.ac.jp)

[toshi@momo.nuae.nagoya-u.ac.jp](mailto:toshi@momo.nuae.nagoya-u.ac.jp)

2. Ballistics and Weapons Concepts Division, AMSRL-WM-BE, Army Research Lab.

Aberdeen Proving Ground, MD, 21005-5066,

[nusca@arl.mil](mailto:nusca@arl.mil)

3. Center for Advanced Numerical Engineering Simulations, School of Mechanical and Production Engineering  
Nanyang Technological University, Singapore 639798,

[mxjwang@ntu.edu.sg](mailto:mxjwang@ntu.edu.sg)

4. French-German Research Institute of Saint-Louis (ISL), 5 Rue du General Cassagnou

F-68301 Saint-Louis, CEDEX, France,

[isl@concorde.cedocar.fr](mailto:isl@concorde.cedocar.fr)

### Abstract

Numerical simulations of the same ramac geometry and initial conditions by different numerical and physical models highlight the variety of solutions possible. The benchmark test was defined and announced within the community of ramac researchers. Three laboratories undertook the project. The numerical simulations include Navier-Stokes and Euler simulations with various levels of physical models and equations of state. The non-reactive part of the simulation produced similar steady state results in the three simulations. The chemically reactive part of the simulation produced widely different outcomes. The original experimental data and experimental conditions are presented. A description of each computer code and the resulting flowfield is included. A comparison between codes and results is achieved.

## 1. Background and definition

Since the beginning of research on the Ram Accelerator problem, a large body of experimental data and numerical simulations has been accumulated. It was suggested that a coordinated effort for a particular experiment and numerical simulation replicated identically by all laboratories could be of use and interest [1]. This project was labeled the Ramac Benchmark Test. This is by definition a numerical simulation based on a successful experiment, but not an attempt to recreate an experiment. The simplifications were specified to allow comparisons between codes, and they limit the scope of a more realistic simulation, but given the variety of computer codes, the limited budget and time available to dedicate to this project, the simpler conditions were preferred to the realistic ones. Given the complexity of this simulation, it can be expected that the outcome can be quite different for each simulation. With that forewarning, the authors volunteered their computer resources and time to perform the simulation following closely the guidelines established, and a comparison of the results has been possible.

The Benchmark is a standard, simple, two-dimensional axisymmetric ramac configuration, avoiding the major complications of fins and three-dimensional effects. It is based on the rail-guided ramac developed at the Institute of Saint-Louis (ISL) [2]. The purpose of the Benchmark is to have a standard configuration that can be used to calibrate a numerical code before attempting a more elaborate simulation.

### 1.1 Selected configuration

The geometry and initial conditions were defined based on a suggestion by Dr. Seiler from the ISL to use

## Numerical Simulation of the Ramac Benchmark Test

J. E. Leblanc<sup>1</sup>, M. Nusca<sup>2</sup>, X. Wang<sup>3</sup>, F. Seiler<sup>4</sup>, M. Sugihara<sup>1</sup>, and T. Fujiwara<sup>1</sup>

1. Department of Aerospace Engineering, Nagoya University,  
Chikusa-ku, Nagoya, Japan 464-8603

[joseph@momo.nuae.nagoya-u.ac.jp](mailto:joseph@momo.nuae.nagoya-u.ac.jp)  
[toshi@momo.nuae.nagoya-u.ac.jp](mailto:toshi@momo.nuae.nagoya-u.ac.jp)

2. Ballistics and Weapons Concepts Division, AMSRL-WM-BE, Army Research Lab.  
Aberdeen Proving Ground, MD, 21005-5066,  
[nusca@arl.mil](mailto:nusca@arl.mil)

3. Center for Advanced Numerical Engineering Simulations, School of Mechanical and Production Engineering  
Nanyang Technological University, Singapore 639798,  
[mxjiwang@ntu.edu.sg](mailto:mxjiwang@ntu.edu.sg)

4. French-German Research Institute of Saint-Louis (ISL), 5 Rue du General Cassagnou  
F-68301 Saint-Louis, CEDEX, France,  
[isl@concorde.cedocar.fr](mailto:isl@concorde.cedocar.fr)

### Abstract

Numerical simulations of the same ramac geometry and initial conditions by different numerical and physical models highlight the variety of solutions possible. The benchmark test was defined and announced within the community of ramac researchers. Three laboratories undertook the project. The numerical simulations include Navier-Stokes and Euler simulations with various levels of physical models and equations of state. The non-reactive part of the simulation produced similar steady state results in the three simulations. The chemically reactive part of the simulation produced widely different outcomes. The original experimental data and experimental conditions are presented. A description of each computer code and the resulting flowfield is included. A comparison between codes and results is achieved.

## 1. Background and definition

Since the beginning of research on the Ram Accelerator problem, a large body of experimental data and numerical simulations has been accumulated. It was suggested that a coordinated effort for a particular experiment and numerical simulation replicated identically by all laboratories could be of use and interest [1]. This project was labeled the Ramac Benchmark Test. This is by definition a numerical simulation based on a successful experiment, but not an attempt to recreate an experiment. The simplifications were specified to allow comparisons between codes, and they limit the scope of a more realistic simulation, but given the variety of computer codes, the limited budget and time available to dedicate to this project, the simpler conditions were preferred to the realistic ones. Given the complexity of this simulation, it can be expected that the outcome can be quite different for each simulation. With that forewarning, the authors volunteered their computer resources and time to perform the simulation following closely the guidelines established, and a comparison of the results has been possible.

The Benchmark is a standard, simple, two-dimensional axisymmetric ramac configuration, avoiding the major complications of fins and three-dimensional effects. It is based on the rail-guided ramac developed at the Institute of Saint-Louis (ISL) [2]. The purpose of the Benchmark is to have a standard configuration that can be used to calibrate a numerical code before attempting a more elaborate simulation.

### 1.1 Selected configuration

The geometry and initial conditions were defined based on a suggestion by Dr. Seiler from the ISL to use

the 30 mm rail-guided experiment with hydrogen fuel diluted with carbon dioxide. The ISL is providing experimental data of the superdetonative shots. The shape, shown in Fig. 1, is a two-dimensional, axisymmetric cone-cylinder-cone without fins, of maximum diameter of 30 mm, and total length of 161 mm, centered in a tube of 44 mm bore diameter. This leaves a gap of 7 mm at the throat. The following initial conditions have been proposed for the simulation: Mixture:  $2\text{H}_2 + \text{O}_2 + 5\text{CO}_2$ , Pressure: 20 bars, Temperature: 300 K, Injection velocity: 1800 m/s

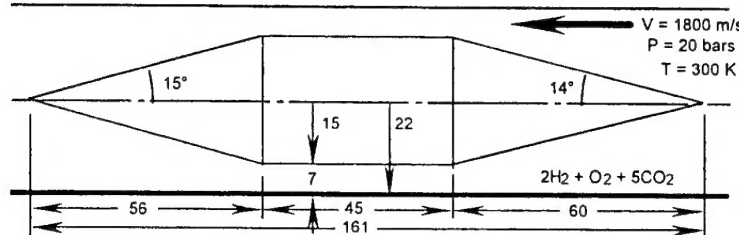


Figure 1. Geometry and initial conditions of the proposed Ramac Benchmark Test.  
All dimensions in millimeters.

The options of governing equations, numerical scheme, grid system, and boundary conditions were left open for each author. The physical models were somewhat restricted; the guidelines suggest that heat transfer, turbulence and diffusion models can be included, if available. The ideal gas equation of state was specified, to avoid discrepancies with various real equations of states, although a comparison between equation of states is desired.

The chemistry was limited to hydrogen and oxygen reactions, using any existing model, but it was specified that carbon dioxide be used strictly as a diluent. The reaction with  $\text{CO}_2$ , will be neglected for this simulation to avoid discrepancies in the simulation from codes with and without a model of  $\text{CO}_2$  combustion. It should be kept in mind that the Benchmark is not a reproduction of an experiment, but a selected model for the purpose of comparing and calibrating our numerical codes, it is only based on a set of experimental conditions.

The following is the original Benchmark definition broadcasted by electronic mail. This was the basis for the simulations performed.

#### The Superdetonative Benchmark Guidelines

##### (1) The ramac shape:

The rail guided, cone+cylinder+cone ( $<==>$ ) projectile used by the ISL. The front cone is 14 degrees half angle, 60 mm long, then a cylinder of 30 mm diameter, 45 mm long, then another cone, of 15 degrees half angle, and 56 mm long. Total mass of 130 grams.

##### (2) The tube:

The tube used at the ISL has five rail guides, and it is almost circular, so let's assume a circular tube of inner bore 44 mm, so the space between body and tube is 7 mm on each side. I'm assuming you will do a 2-D axisymmetric simulation, so I'm not giving you details of the tube cross section. If you want to do a 3-D simulation, with rail guides and all, I will send you more details.

##### (3) The initial conditions:

Injection velocity: 1800 m/sec. Pressure: 20 bar. Temperature: 300K. Fuel mixture:  $2\text{H}_2 + \text{O}_2 + 5\text{CO}_2$   
What chemical model to use? Use whichever hydrogen model you already have coded in your chemistry subroutine. I don't know how reliable the existing models are at high pressures, but let's use what we have. To keep it simple and allow comparisons, let's not include the carbon dioxide reactions in the chemical model. Use the carbon dioxide as an inert diluent.

##### (4) The grid:

Up to you to design the grid system most appropriate for your code.

##### (5) The boundary conditions:

Tube wall: Adiabatic. Projectile body: Depends on the physical model you have implemented. The projectile

body boundary conditions are another important point that might affect the results. If you use a Navier Stokes code, the BC is non-slip, with heat transfer. If you use an Euler code, the BC is slip, and maybe adiabatic. The material is an aluminum magnesium copper alloy (Dural alloy).

(6) The equation of state:

If you have a real gas equation of state for high pressure, please use it. If you only have the ideal gas EoS, use it, it is good as a first approximation. That's one point I would like to see a comparison.

(7) The physical models:

If you have a heat transfer model, use it. If you have a turbulence model, use it. If you have a diffusion model, use it. But I don't think they will have much influence because the gas is premixed, the space where the reaction takes place is very narrow, the time scale is very short, and the flow speed is supersonic.

(8) The detonation initiation:

This mixture will burn easily with those conditions, so it should detonate quickly. Don't worry about diaphragms at this stage, we only want to see a steady state solution.

---

## 2. Overview of the Results

The results are presented in four parts: First the experimental data from the ISL, selected for the benchmark defining conditions. Then the numerical results by Nusca, by Wang, and finally by Leblanc. The following comments try to summarize the similarities and differences between the three simulations.

The grid systems used are similar in shape. Nusca has 314x40 points uniformly spaced. Wang has 141x48 grid points clustered near the ramac body. Leblanc has 430x100 points with higher density of points in the midbody section, and uses generalized coordinates conforming to the front nose. This grid guarantees radial grid lines normal to the body, and is more appropriate for boundary conditions.

The results of non-reactive simulation (also called inert by Nusca, and cold flow by Wang) shows similar patterns of shock reflections and interactions, but the peak pressure and temperature levels are different for the three simulations. The peak pressure of the first reflected shock wave for Nusca is  $25P_0$ , for Wang it is  $6P_0$ , and for Leblanc it is  $14P_0$ , where  $P_0$  is the fill pressure of 20 bars. These cannot be compared with the experimental data, which has combustion. A common characteristic in all simulations is that the expansion fan generated at the projectile shoulder intersects the reflected shock, and the shock weakens and bends.

The results of the chemically reactive simulation shows even greater differences in the initiation, patterns and pressure levels. The only difference between non-reactive and reactive case is the source of energy from the exothermic chemical reaction.

Nusca used a Navier-Stokes code with a detailed model of hydrogen combustion. Autoignition occurred at the wall and body and the combustion was steady. The pressure peak pattern and levels on the wall are similar to the experimental results ( $60 P_0$ ). Nusca uses a co-volume equation of state, while Wang and Leblanc use ideal gas equation of states.

Wang used a Navier-Stokes code, with a chemical kinetics model of  $H_2/O_2$ /diluent combustion with 8 reactions and 7 species. Autoignition occurred at the rear point ( $x = 170$  mm) and moved forward along the boundary layer. Eventually the combustion moved to the front cone and became a stable oblique detonation wave supported by the cone. The pressure level on the throat section is similar to the experimental level ( $60P_0$ ), although the pattern of peak pressures and reflections is different.

Leblanc used an Euler code, with a chemical kinetics model of  $H_2/O_2$ /diluent combustion with 19 reactions and 8 species, and the ideal gas equation of state. There was no auto-ignition anywhere, even though the pressure and temperature levels were as high as in Wang's simulation. Even after igniting the mixture, it could not support combustion, so the amount of diluent was reduced to three moles  $CO_2$  to make it more energetic. After forced ignition, it supported a steady combustion. The pressure level on the wall is low by a factor of two ( $47P_0$ ). The reason for this low pressure is not apparent, but it does not seem due to the ideal gas equation of state because Wang used the same EoS and obtained high pressures.

### 3. Experimental Data from Seiler

Seiler provided the suggestion for the appropriate superdetonative benchmark conditions and the experimental data to compare with the simulations. The data supplied was of experiments numbered 197, 222, 224, and 225. We selected No. 222, and show that data in Fig. 2. The following description was also provided.

The experiments were performed with the rail guided ramac version II, using hydrogen as fuel and CO<sub>2</sub> as diluent. The tube is 4.8 meters long, with a cross section of five rails supporting the 30mm cone-cylinder ramac. Injection velocity at x = 0: 1810 m/sec. Fill pressure: 20 bar. Fuel mixture: 2H<sub>2</sub> + O<sub>2</sub> + 5CO<sub>2</sub>. Projectile mass: 30 g. The pressure records in Fig. 2 are for the canal transient recorders ADAM in stations M6, M8, and M10, coupled with the position of the projectile shape. The data on projectile position and velocity along the tube is shown in Table 1. The position is the location at which the projectile speed is calculated as the mean value between two sensors. The velocity is given by the electromagnetic sensors.

| CANAL<br>ADAM | Location [mm] | Speed [m/s] |
|---------------|---------------|-------------|
| M4            | 300.42        | 1826.26     |
| M5            | 900.62        | 1841.97     |
| M6            | 1500.325      | 1868.69     |
| M7            | 2100.535      | 1906.57     |
| M8            | 2700.395      | 1923.43     |
| M9            | 3299.905      | 1925.75     |
| M10           | 3899.92       | 1972.91     |
| M11           | 4431.155      |             |
| M12           | 5213.87       |             |
| M13           |               |             |

Table 1. Data for experiment number 222.

Notice the variations in the peak pressures at different stations. The plot from station M6 was selected as the representative one, to be used for comparisons, and was digitized by Nusca. The pressure as a function of time is converted to a function of distance using the projectile velocity. That pressure data is included in the pressure line plots by Nusca and Leblanc (Figs. 6, 9, 11, and 28)..

### 4. Simulation by Nusca

#### 4.1 Description of the ARL CFD code

The CFD computations performed at the US Army Research Laboratory (ARL, by M.J. Nusca) utilize a numerical simulation code developed for chemically reacting flows. This CFD code solves the unsteady, 2D/axisymmetric Navier-Stokes equations including species diffusion, thermal conduction, viscosity, and nonequilibrium chemical kinetics [3,4,5]. The various transport properties are represented using binary diffusion coefficients, curve-fitted data and mixing laws. A conservation equation for each chemical species is included in the flow equations and requires chemical production terms. Given an appropriate chemical kinetics mechanism, defining the species, reactions, and reaction rates, these terms can be computed. For this purpose a H<sub>2</sub>/O<sub>2</sub>/CO<sub>2</sub> mechanism was installed in the CFD code. This mechanism (22 species and 32 reactions; CO<sub>2</sub> is inert) was assembled at Stanford University and was previously used to validate the ARL code [4]. The

reaction rates follow an Arrhenius formulation with forward rates specified and backward rates computed using the equilibrium constant. Some reactions account for the dependence on high pressures. The conservation equations are closed with an equation of state and a turbulence model. A co-volume equation of state is used to determine pressure from the density, temperature and molecular weight at each point in the flowfield. Flow turbulence is modeled using a mixing-length equation, with the precise location of onset prescribed for each solid wall. Walls are considered isothermal. The conservation-law form of the flow equations is used and a finite-volume discretization methodology is employed. The convective and transport fluxes are resolved using upwind and central-differencing, respectively, along with flux-limiting methods. See References 3, 4 and 5 for more details.

#### 4.2 Discussion of ARL results for the inert flowfield

Figure 3 shows the computational grid used for the ARL CFD simulations. There are 314 grid cells in the axial direction and 40 grid cells in the radial direction (note that the figure shows every other grid cell). The grid is essentially uniform in each direction with some radial grid clustering near the tube wall and the projectile surface wall. The wall grid spacing is approximately 0.07 mm which is considered more than adequate for inviscid flow simulations and satisfactory for viscous flow simulations (the turbulence model follows a law-of-the-wall methodology). All dimensions follow those used in the ISL ramaccelerator. The projectile nosetip is pointed, as is the projectile base. A grid region that is 4 mm long was placed in front of the projectile nosetip and 10mm section was placed behind the projectile base.

The inflow is prescribed in accordance with the conditions of Shot 222 of the ISL. The outflow is assumed supersonic for inviscid flow simulations with boundary condition corrections applied for viscous simulations in the thin boundary layer region on the tube wall and the projectile wake region near the tube centerline. The wall boundary conditions are no-penetration for inviscid and no-slip for viscous simulations with isothermal and non-catalytic conditions imposed as well. The tube wall is considered adiabatic, and the projectile surface isothermal (constant temperature of 500K). The reason is that some heating (from 300K to 500K) is expected before entrance into the ramac tube, but time-of-flight through the ramac tube is too short for further heating. There is a temperature gradient at the projectile surface, but none at the tube wall.

Computations are done in the projectile-fixed reference frame assuming a constant flow velocity (i.e., the inflow and the tube wall are assumed to be moving at the prescribed projectile velocity). As a direct result, a boundary layer will not form on the tube wall until the bow shock from the projectile reflects from it (for viscous flow simulations). The small sections of tube centerline ahead of and behind the projectile are treated as an axis of symmetry.

Figures 4, 5 and 6 show results for the inviscid, inert flowfield. The projectile bow shock reflects from the tube wall at about 70mm from the grid origin as indicated by a sharp rise in temperature (Fig. 4) and pressure (Fig. 5 and 6) at this point. Pressure is nearly constant on the projectile forebody compression and decreases in the flow expansion onto the midbody (Fig. 6). The bow shock reflection is slightly curved due to its interaction with the expansion wave generated at the projectile forebody-midbody junction and intersects the projectile near the end of the midbody (Fig. 4 and 5). Note the pressure rise on the projectile surface at about 100-110 mm (see Fig. 6). This shock reflects again and is severely weakened in the expanding afterbody flowfield. It intersects the tube wall at about 150mm (note the small pressure rise in Fig 6 at this location). A strong recompression is noted at the projectile base along the axis (Fig. 4, 5 and 6). The computed pressure distribution is not in very good agreement with the tube wall data (Fig. 6) since these data were taken in the reactive flow environment.

Figures 7, 8 and 9 show results for the viscous, inert flowfield. Laminar boundary layers are permitted to naturally form on the tube wall and the projectile walls. Note the thick regions of higher temperature on the walls in Fig. 7. The boundary layer on the projectile forebody is very thin and does not cause noticeable changes to the pressure and temperature fields as compared to the inviscid results. Observations of laminar boundary layer thickening on the projectile midbody surface, after the flow expansion, prompted the choice to let the boundary layer become turbulent at the axial location of about 75mm (see Fig. 9). For consistency, this location was also used on the tube wall (i.e., about 5mm downstream of the bow shock reflection point). For both surfaces, the transition to turbulence causes a small shock to form (Fig. 7 and 8) as indicated by a pressure increase on both walls at about 80mm (see Fig. 9). Like for the inviscid flowfield, the projectile bow shock reflects from the tube wall at about 70mm from the grid origin as indicated by a sharp rise in temperature (Fig. 7) and pressure (Fig. 8 and 9) at this point. The bow shock reflection is more highly curved due to its interaction with the expansion wave generated at the projectile forebody-midbody junction and the small shocks generated on the body and on the tube at the location of boundary layer transition. The resultant shock intersects the projectile farther from the end of the midbody (Fig. 7 and 8). Note the larger pressure rise

on the projectile surface at about 105mm (Fig. 9). This shock reflects again and is weakened in the expanding afterbody flowfield (Fig. 8). It intersects the tube wall at about 120mm (note the pressure rise in Fig. 9 at this location). A strong recompression does not occur at the projectile base along the axis (as is the case with inviscid flow, see Fig. 5) due the thick boundary layer from the projectile afterbody (Fig. 7). The computed pressure distribution is in better agreement with the tube wall data (Fig. 9) as compared to the inviscid result (Fig. 6). The double pressure spike computed between 70 and 90mm begins to approach the measured pressure levels. Smaller computed pressure increases at 102 and 120mm seem to mimic the pressure data trends at these locations.

#### 4.3 Discussion of ARL results for the Reacting flowfield

Figures 10, 11 and 12 show pressure results for the viscous, reacting flowfield. Comparing Fig. 8 (viscous, inert flow) and Fig. 10 (the contours have been purposely plotted using the same limits) one can observe regions of higher pressure on the tube wall in a generally similar pattern or distribution. The same can be said for the projectile surface except that on the afterbody the pressures are not only higher for reacting flow but the distribution is not as characteristic of simple flow expansion. Rather, the afterbody pressures for reacting flow are more concentrated on the surface due to the heat release of combustion. Fig. 11 shows the pressure distributions and Fig. 12 compares the projectile surface pressure distributions for inert and reacting flow. Comparing Fig. 9 (viscous, inert flow) and Fig. 11 (the pressure axis has been purposely plotted using the same limits) one can observe a very similar pressure rise between 70 and 75mm (due to the reflection of the projectile's bow shock on the tube wall) and a marked increase in pressures on the tube wall after that point. This is due to combustion. Note the similarities between computed and measured tube wall pressures, displayed in Fig. 11, with the exception of the region near 105 mm. Here we see a measured pressure rise to about 60 with no corresponding computed pressure peak. It could be that the computations are shifted in the axial direction for some reason since the computations do show a comparable pressure rise at 120mm on the tube wall (more will be said about this below). Fig. 12 highlights the computed increase in pressure on the projectile surface due to combustion. In particular, the reacting flow, relative to the inert flow, shows very slight increases in pressures on the forebody, where the projectile generates a drag force, but marked increase in pressure on the afterbody, where the projectile generates thrust. Note in Fig. 12 that the forebody and afterbody pressures are nearly the same for inert flow but that the afterbody pressure is notably higher than the forebody pressure for the reactive flow. This is of course where the ramaccelerator concept provides its propulsive mechanism.

Figures 13 and 14 show the computed mass fraction contours and surface distributions for the species OH. The OH radical (along with the H<sub>2</sub>O molecule) is noteworthy since it is formed during heat release in H<sub>2</sub>/O<sub>2</sub> combustion. Plotted results for H<sub>2</sub>O are qualitatively similar those of OH (other species such as HO<sub>2</sub> and H<sub>2</sub>O<sub>2</sub> form behind the projectile's bow shock and subsequent shocks reflected from the tube wall to the projectile). Very small levels of OH are observed on the projectile forebody with significant concentrations found in the hot wall boundary layers. The mass fraction of OH in the space between the projectile and tube walls is smaller than 0.001. The qualitative pattern of the OH contours, seen in Fig. 13, is strikingly similar to that photographed in the Stanford University expansion tube (when testing bodies of similar shape in H<sub>2</sub>/O<sub>2</sub> flow conditions typical of ramaccelerator operation) and computed using the ARL CFD code (see Reference 4).

For Fig. 14, it is interesting to note that the levels of OH on the projectile surface and on the tube wall are similar except for a significant reduction in OH on the tube wall between 95 and 115mm. The cause of this reduction is unclear without further investigation but the associated reduction in heat release causes a lower than expected pressure in this region (see Fig. 11).

### 5. Simulation by Wang

#### 5.1 Numerical Algorithm and Chemical Models.

The CFD program was developed which solves the 2D/Axisymmetric Reynolds-Averaged Navier-Stokes equations coupled with Baldwin-Lomax turbulent model. The Yee-Harten symmetric TVD scheme is employed and the chemical kinetics is included into the conservation equations. The LU-SGS algorithm is applied to solve the implicit scheme. The diagonal implicit source term used by Eberhardt and Imlay [7] are employed. NS equations can be simply expressed as:

$$\frac{\partial Q}{\partial t} + \frac{\partial(E - E_v)}{\partial \xi} + \frac{\partial(F - F_v)}{\partial \eta} + \alpha(H - H_v) = W$$

The detail definitions for above parameters refer to [6], [7]. The chemical reactions are introduced using 8 reactions in 7 species, chemistry kinetics model [8]. This model is simple and easy to be coupled with CFD code. For H<sub>2</sub>/O<sub>2</sub>/diluent gas mixture, it is also sufficient to model the combustion temperature, except the ignition process.

## 5.2 Calculation Results and Discussions

The calculation parameters are the same as that given in RAMAC-IV benchmark test. The 141x48 grids are chosen in the calculation domain. In the following calculations, the projectile temperature is fixed, T(surface) = 500K, the pressure gradient at the surface is set to zero, and the density calculated by EoS ( $\rho = P/RT$ ), so there is a temperature gradient. For the tube wall, the adiabatic condition is applied, so there are no gradients for T,  $\rho$ , or P. All following calculation results are obtained under the steady-flow assumption.

Figure 15 shows the calculation domain and grids of the flow field (2 times magnitude in y direction). Figure 16 gives the pressure distribution along the tube wall and the surface of the projectile body under cold flow condition (combustion is switched off). The pressure is normalized by initial pressure  $P_0$  (20 atm); the distance X (along projectile axis) is normalized by the radius of launcher tube.

Under cold flow assumption, the highest temperature is around 1000 K on the rear nose region, see Fig. 18. The highest pressure, 6.06  $P_0$ , is located on the wall of tube, see Fig. 16 and Fig. 20. The thrust coefficient,  $C_f (=F/(P_0A))$ , is -2.205, which include -1.02 of viscous drag coefficient. Figure 19 shows the temperature contours of the reactive flow. The highest combustion temperature reaches 3050 K. The H<sub>2</sub>O and OH contours are shown in Figs. 22 and 23, respectively.

The pressure distributions of the combustion flow field are presented in Fig. 17. The pressure contours are given in Fig. 21. The pressures on tube wall and on the surface of the projectile reach up to 60  $P_0$ . This highest pressure is located in the region of the cylinder body.

The ignition happens on the rear nose area and then moves to the rear part of the body along the boundary layers. Ignition process is fairly slow; combustion finally moves to the front nose of the projectile. The thrust coefficient is 2.896, including viscous drag coefficient -0.099. This value is different from the thrust coefficient in shot 222, which is 3.42, see the experiments in ISL [9].

Comparing to experiments, the highest peak pressure of the numerical calculation is in good agreement with the experimental result. In this calculation, the combustion moves forward to the surface of the nose cone of the projectile. However, according to the experimental results, the locations of the combustion wave and the peak pressure are located on shoulder and cylinder body and no any combustion exists in the region of the nose cone.

Since the combustion and ignition are a slow process in this calculation, the time scale of combustion might have the same order compared with the time scale of the projectile flight, so the experimental results might not be steady state.

It is found that the  $C_f$  reaches a value of 4.0 or even higher during the numerical calculation process, before it reaches convergence (steady state solution). The final results of the steady-flow field may not reflect the realistic results in the experiments. However, the calculation process and final results give us a possible range of the parameters (P, T etc.) quantitatively. The effects on the combustion flow field are also attributed to the parameters, such as viscosity of the flow, chemical reaction schemes, and grids.

## 6. Simulation by Leblanc

### 6.1 Description of the numerical code

The computer program was developed for simulation of shock-induced detonations by a hemisphere cylinder body, and also used for simulations of Ram Accelerator. It solves the inviscid Euler equations to second order in space and time, by capturing the shock wave in a two-dimensional, axisymmetric curvilinear grid system. The equations are solved explicitly using the Harten-Yee TVD scheme, with a non-MUSCL method of interpolating the fluxes, and Roe's method to average the fluxes between grid points. A metric Jacobian converts the curvilinear coordinate system into the computational domain. The equation of state is

the law for ideal gases, where the pressure  $P(T, \rho)$  is a function of temperature and mass density. The thermodynamical characteristics ( $c_p, s_i, h_i$ ) are calculated from polynomial functions of temperature. The program does not include physical models of heat transfer, diffusion, or turbulence because the time scales of the experiment and the simulation are small compared to the time scales of the respective phenomenon.

The chemistry is solved implicitly and it uses Jachimowski's [10] model of 19 reaction in 9 species for gaseous detonation of hydrogen and oxygen. This means a subset of the original chemical kinetics model, obtained by eliminating the reactions containing nitrogen. This model has been used repeatedly in our laboratory for numerical simulation of this type [11,12,13].

The simulations were performed with the grid shown in Fig. 24. It consists of 430x100 points. This grid has a rounded nose tip, and the radial grid lines are perpendicular to the projectile front cone. From a physical point of view, this grid is closer to a real projectile with a slightly blunted tip, and the normal grid lines allow a more proper treatment of the boundary conditions. The boundary conditions at the projectile body use a two-grid cell extrapolation of the velocity vector to the wall grid point, and recalculate the energy density variable at the wall. The boundary conditions at the tube wall use a simple one-grid cell reflection. Both are slip and adiabatic; the wall is allowed to take the flowfield temperature.

## 6.2 Methodology and results

We performed a grid refinement study to determine a suitable number of grid points. The blunted cone grid was tested in the non-reactive case for the following values: 270x80, 430x100, 750x100, and 1500x200. The grid point distribution was not uniform, and from this study we could determine which areas needed more or less points. For example, the forward cone was properly resolved with fewer points along the body, but needed more points in the radial direction to resolve the rise in density from the shock compression. The grid points are more densely packed in the midbody cylinder because the reaction zone is expected there. The resolution at the throat was 280  $\mu\text{m}$  axially by 70  $\mu\text{m}$  radially.

Figure 25 shows the non-reactive flowfield, which looks physically reasonable, and the values were verified by analytical means. Notice the shape similar to Nusca's inviscid (Figs 4 and 5) and Wang's viscous (Fig. 20) flowfields. The weak pressure at the wall reflection point could be caused by the intersection of the reflected shock by the expansion wave generated at the projectile shoulder. Plots of the pressure on wall and body are shown in Fig. 26, which compares with Nusca (Fig. 6) and with Wang (Fig. 16) except on the pressure levels.

The pressures and temperatures were too low to initiate or support combustion. Recent simulations by Choi, Taki and Sasoh (specific references are deferred to a published paper) have shown the importance of diaphragm interactions for ignition. We simulated an ignition by feeding extra energy into a vertical strip ahead of the reflected shock, thereby raising the temperature and causing a sudden burst of energy, like from a ruptured diaphragm. The steady state flowfield could not support the combustion and the resulting combustion wave moved downstream, expanded in the back cone, and was washed away from the numerical grid by the incoming flow.

Next we tried a more energetic mixture by lowering the amount of diluent from 5 moles to 3 moles of  $\text{CO}_2$ . Still no auto-ignition, but this mixture could support the detonation wave after ignition. The resulting detonation wave is shown in Fig. 27, where the difference is that the mixture is  $2\text{H}_2 + \text{O}_2 + 3\text{CO}_2$ . Two standing normal shock waves seem to intersect in the center of the throat. The reflected wave pattern is completely changed, and the area behind the detonation and close to the body is subsonic. The highest temperature (3120 K) is in this subsonic area. The temperature and pressure indicated in the figure is the peak at the tube wall.

The comparison with the experimental data is shown in Fig. 28, where the pressure on the wall and body are plotted. The peak value is 50% lower than the experimental data at M6, but it is 30% lower than the peak at M10 (Fig. 2). The second combustion zone is not observed in the plot because the detonation wave has completed the chemical reaction, and disrupted the reflection patterns downstream. Evidence of the completed reaction is found in the contour plots of OH and  $\text{H}_2\text{O}$  mass fraction in Figs 29 and 30. The OH radicals remaining are distributed uniformly in the flowfield, with some gradients near the projectile body. The plot in Fig. 30 can be compared with Nusca (Fig. 14) and Wang (Fig. 23), although they are lower in magnitude to Nusca, but similar levels with Wang, but those are uniform trends in these results.

Finally, following Nusca's Fig. 12, we plot the pressure on the projectile body before and after chemical reaction, and find that the net result is an increase in pressure on the afterbody, with no effect on the forebody, so this simulation produces a net thrust on the ramjet projectile.

## 7. Observations

The following general remarks can be made about these results.

- The non-reactive part of the simulation produces a steady-state flowfield which is similar for all simulations. The chemical reaction, coupled with the physical models, has a strong effect on the outcome.
- The difference in equation of state could explain the difference in peak pressure levels, but had no effect on the overall flow pattern.
- An Euler code simulation is not capable of producing self-ignition, the combustion had to be initiated.
- The Navier-Stokes simulation had self-ignition, perhaps due to the boundary layer, which allows the flow to remain longer than the induction time period before being convected away.
- One Navier-Stokes simulation had a steady state solution with a detonation wave behind the first reflected shock, the other simulation had a steady state oblique detonation wave supported by the cone.

These results show the variety of solutions possible from a similar set of initial conditions, but with various levels of physical models and numerical schemes. It does not invalidate the numerical simulation, but illuminates the strengths and limitations inherent.

## References

- [1] Leblanc, J.E., Fujiwara T., Numerical Simulation of the RAMAC Benchmark Configuration. In: Takayama K. (ed.) *Proc 3rd Int Workshop on Ram Accelerators*, Sendai, July 16-18, 1997.
- [2] Seiler F., Patz, G., Smeets, G., Srulijes, J., Presentation of the rail tube version II of ISL's RAMAC 30. In: Takayama, K. and Sasoh, A. (eds.) *Ram Accelerators*, Springer-Verlag, Heidelberg, pp. 79-87.
- [3] Nusca, M.J., "Computational Simulation of Starting Dynamics in a Ram Accelerator," AIAA Paper 98-3146, July 1998.
- [4] Nusca, M.J., Dinavahi, S.P.G., and Soni, B., "Grid Adaptation Studies for Reactive Flow Modeling of Propulsion Systems," AIAA Paper 99-0970, Jan. 1999.
- [5]. Nusca, M.J., "Numerical Simulation of Electromagnetic Wave Attenuation in Nonequilibrium Chemically Reacting Flows", Computers and Fluids, Vol. 27, No. 2, 1998, pp. 217-238.
- [6] Yoon,Seokkwan and Sameson,Anthony (1988) *Lower-Upper Symmetric-Gauss-Seidel method for the Euler and Navier-Stokes Equations*, AIAA J. Vol 26,No.9,pp.1025-1026.
- [7] Eberhardt, Scott and Imlay,Sott(1992), *Diagonal Implicit Scheme for Computing Flows with finite Rate Chemistry*, J. of Thermophysics and Heat Transfer, Vol.6,No.2,pp.208-216.
- [8] Evans, J.S. and SchexnayderJr, C. J. (1980), *Influence of Chemical Kinetics and Unmixedness on Burning in Supersonic Hydrogen Flames*, AIAA Journal,Vol.18, pp.188-193.
- [9] Seiler, F. Patz, G. Smeets, G and Srulijes, J. (1998), *Influence of projectile material and gas composition on superdetonative combustion in ISL's RAMAC 30*, AIAA paper 98-3445, July 1998.
- [10] Jachimowski CJ (1988) An analytical study of the hydrogen-air reaction mechanism with application to scramjet combustion. NASA TP-2791.
- [11] Leblanc JE, Lefebvre MH, Fujiwara T (1996) Detailed flowfields of a RAMAC device in H<sub>2</sub> - O<sub>2</sub> full chemistry. Shock Waves 6:85-92
- [12] Lefebvre MH, Fujiwara T (1995) Numerical modeling of combustion processes induced by a supersonic conical blunt body. Combustion and Flame. 100: 85-93.

[13] Matsuo A, Fujii K, Fujiwara T, (1995) Flow features of shock-induced combustion around projectiles traveling at hypervelocities. AIAA Journal, Vol. 33, No. 6, pp. 1056-1063.

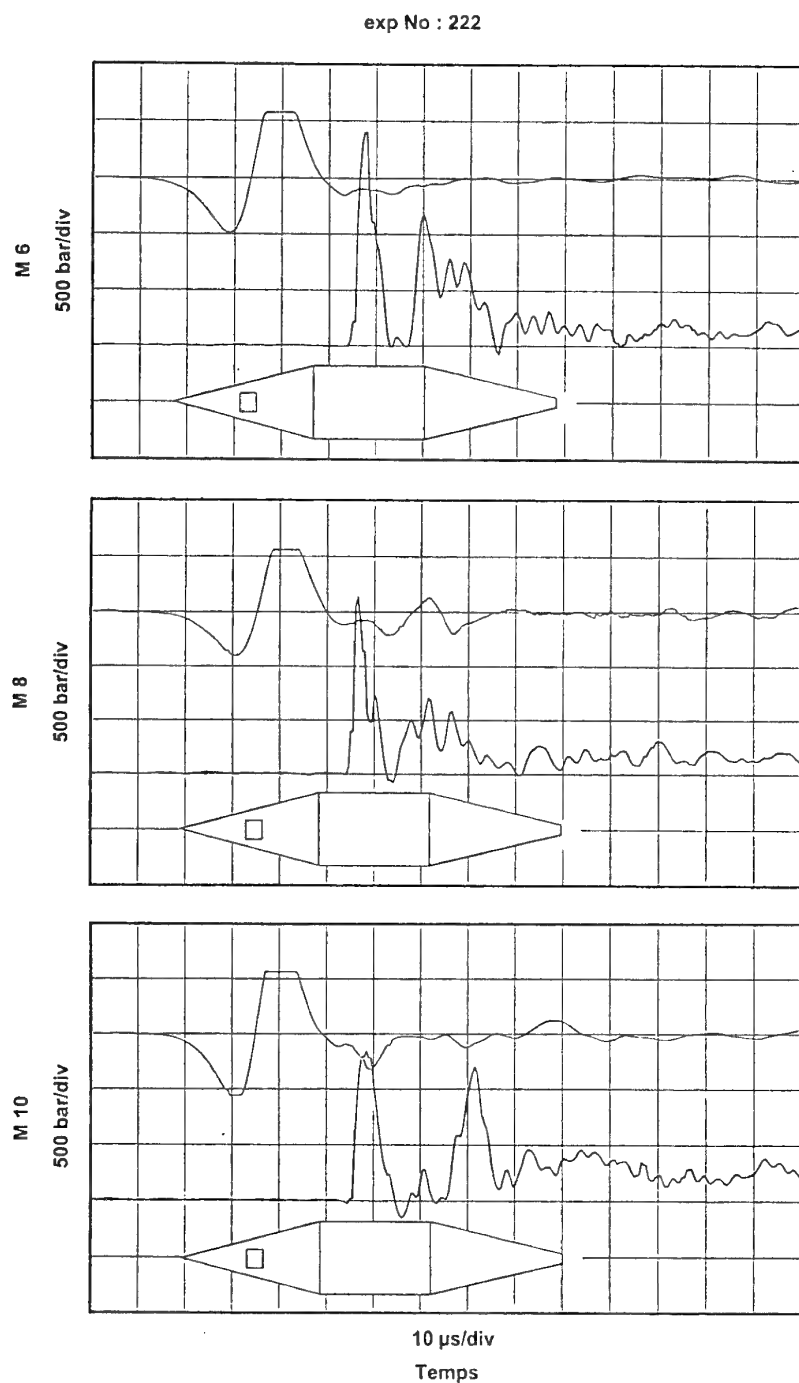


Fig. 2 Experimental data used for defining benchmark initial conditions. Pressure at station M6 is used to compare with simulation results. Fill pressure  $P_0 = 20$  bars. Peak pressures are M6:  $92P_0$ , M8:  $80P_0$ , M10:  $68P_0$ .

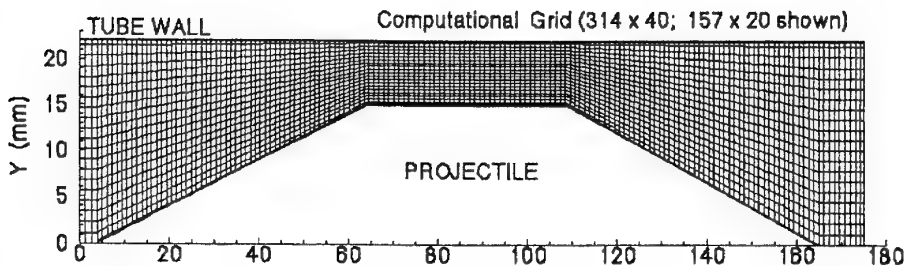


Fig 3. Grid system used by Nusca for both inviscid and viscous numerical simulation.

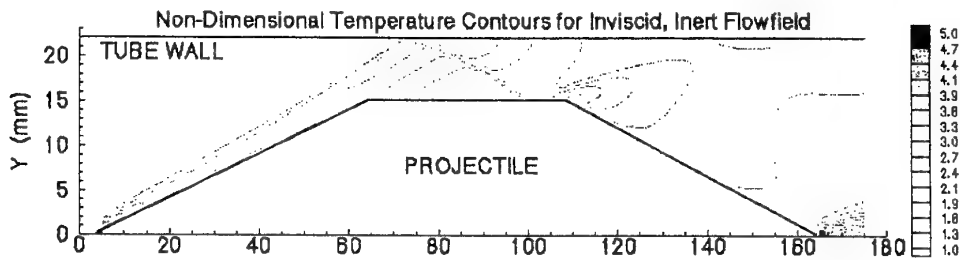


Fig 4. Temperature contour plots, inviscid, inert

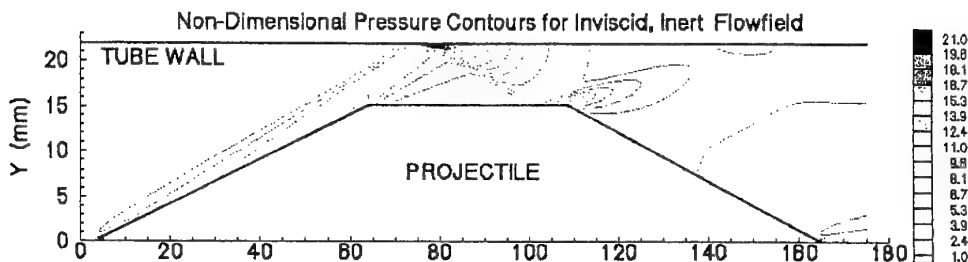


Fig 5. Pressure contour plot, inviscid, inert

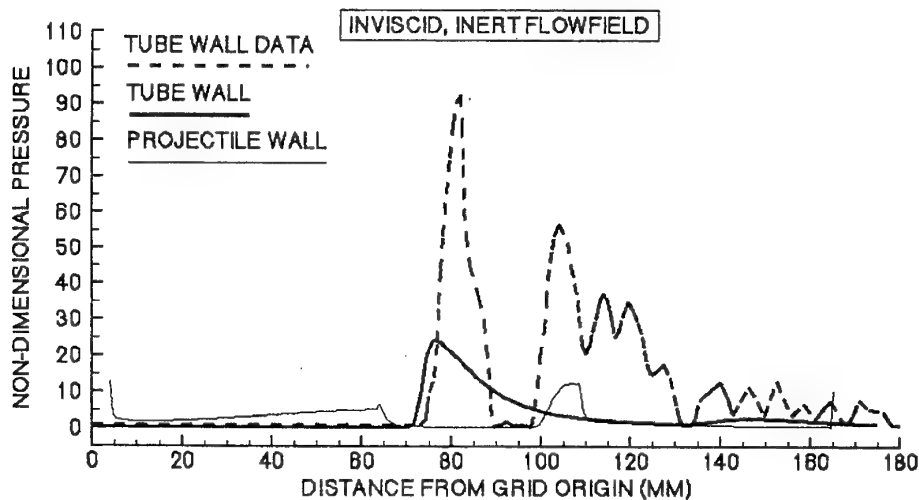


Fig 6. Pressure on tube wall and projectile from simulation compared with experimental data (tube wall data) of station M6 of Fig. 2

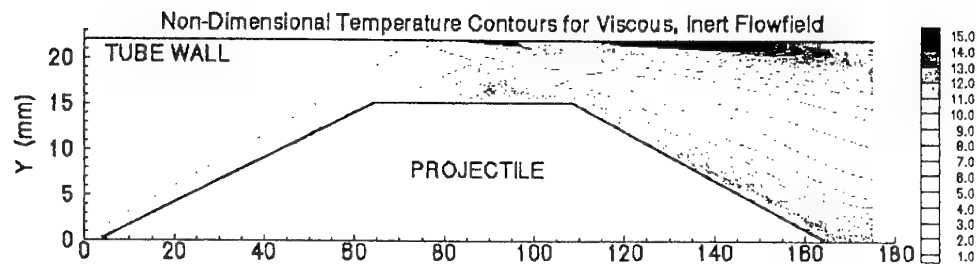


Fig 7. Temperature contours, viscous, inert

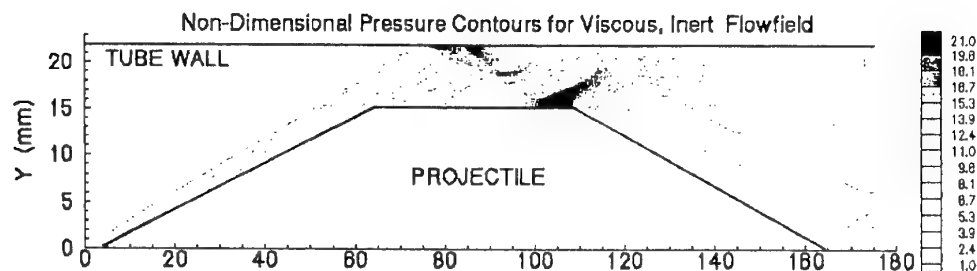


Fig 8. Pressure contours, viscous, inert

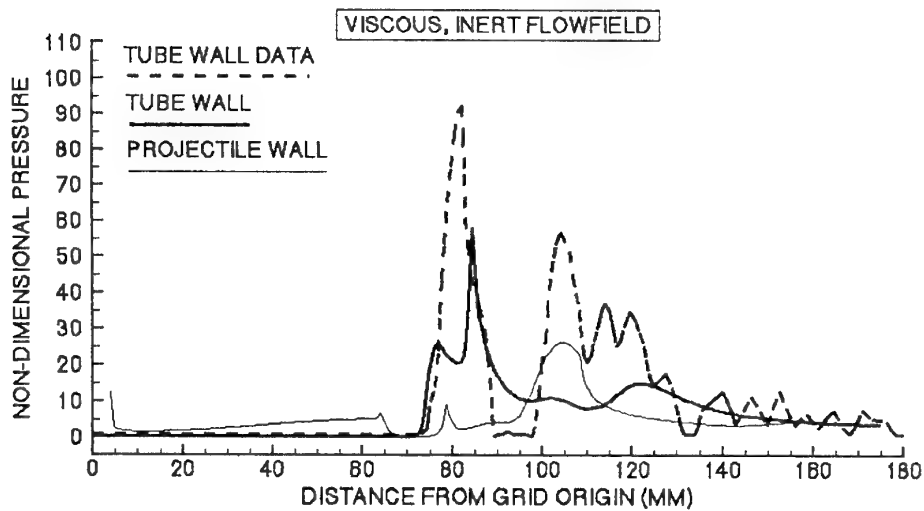


Fig 9. Pressure on tube wall and projectile from simulation compared with experimental data (tube wall data) of station M6 of Fig. 2

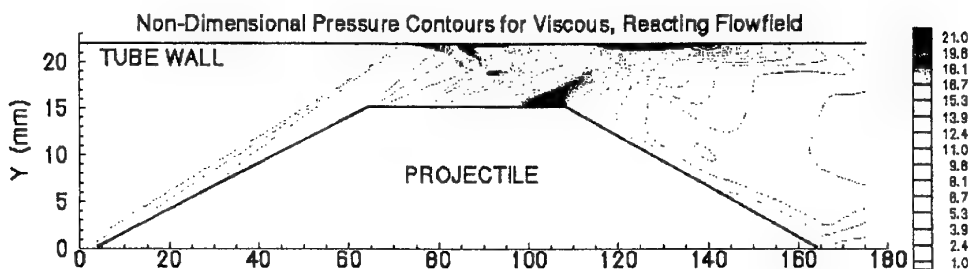


Fig 10. Pressure contours, viscous, reactive

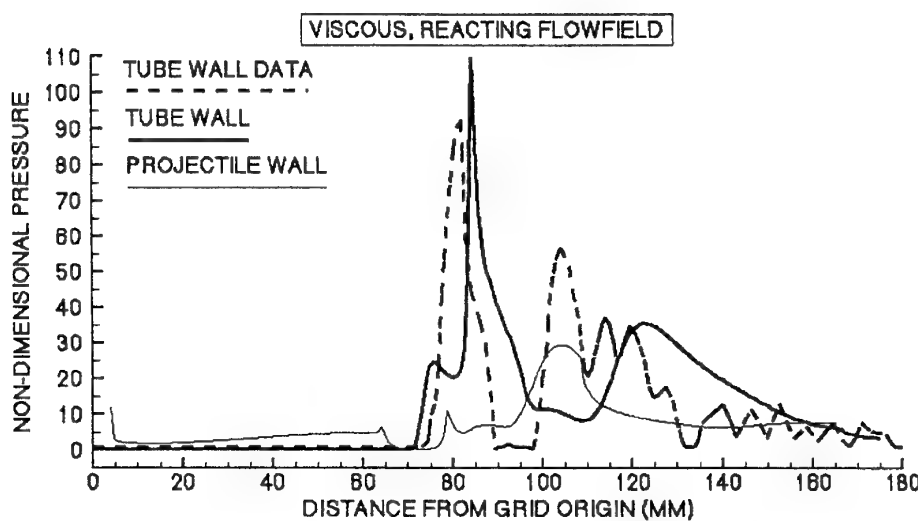


Fig 11. Pressure on tube wall and projectile from simulation compared with experimental data (tube wall data) of station M6 of Fig. 2

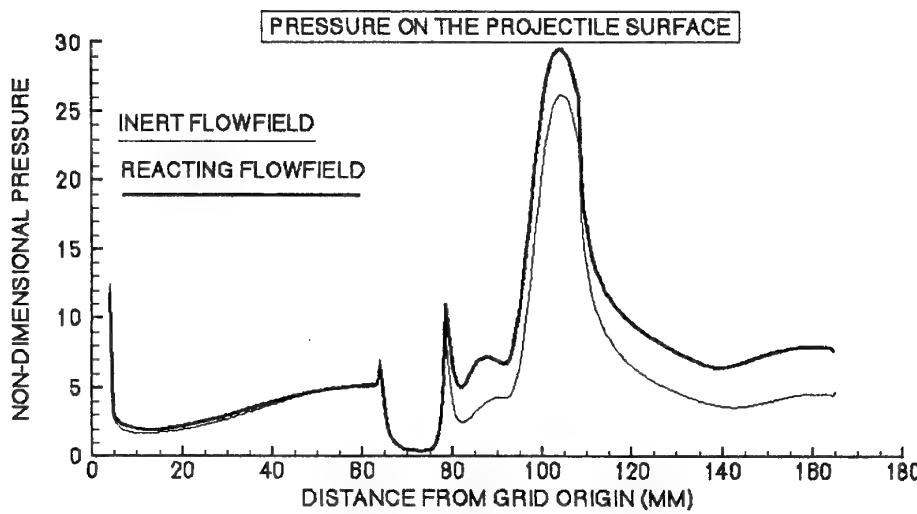


Fig 12. Pressure on the projectile surface, before and after chemical reaction takes place

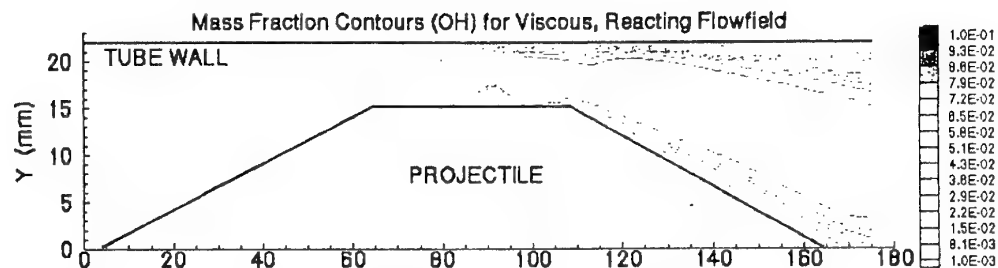


Fig 13. OH mass fraction contours, viscous, reactive

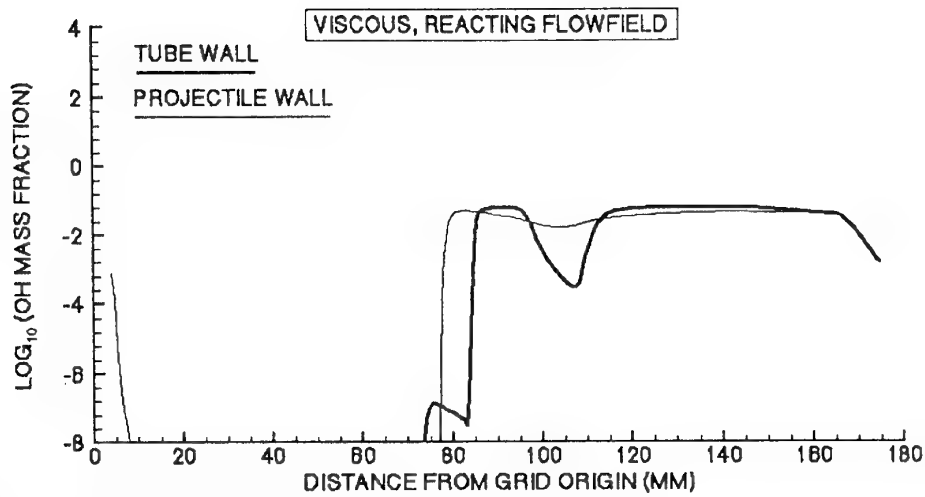


Fig 14. Plot of OH mass fraction on tube wall and projectile

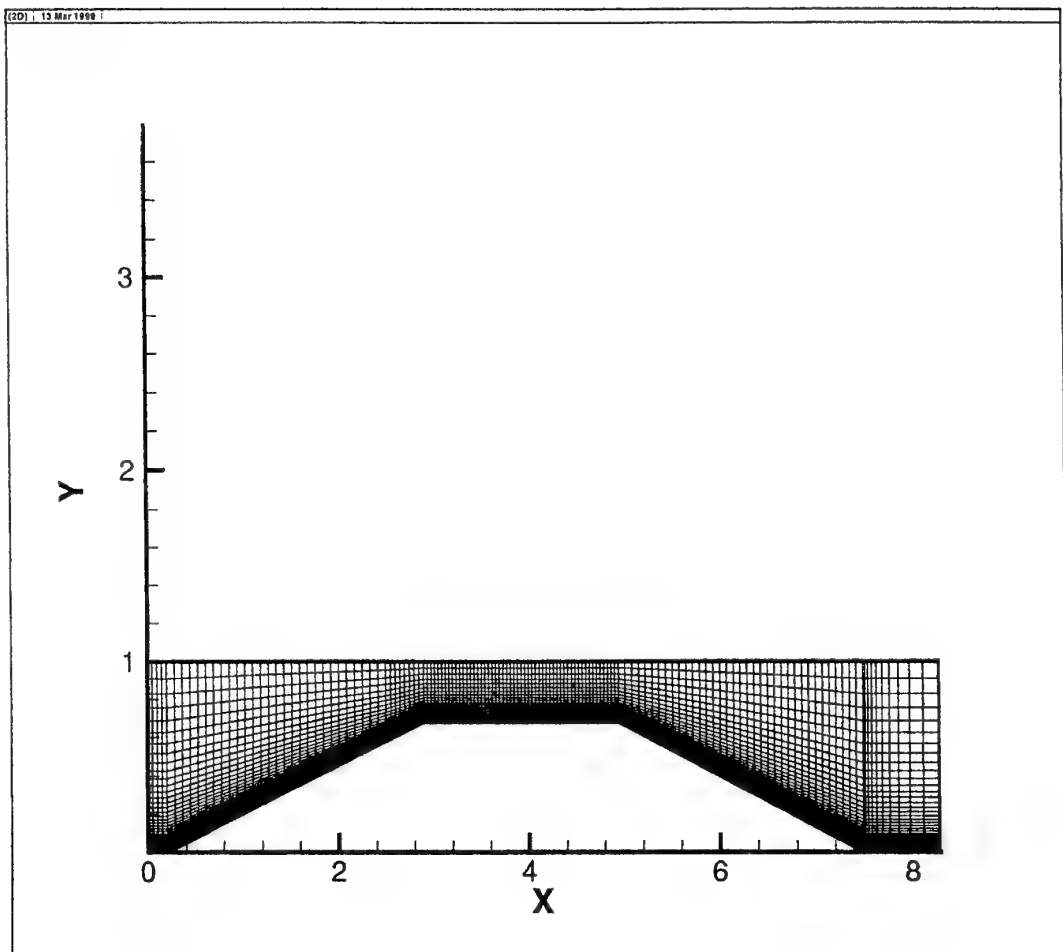


Figure 15: Calculation Domain

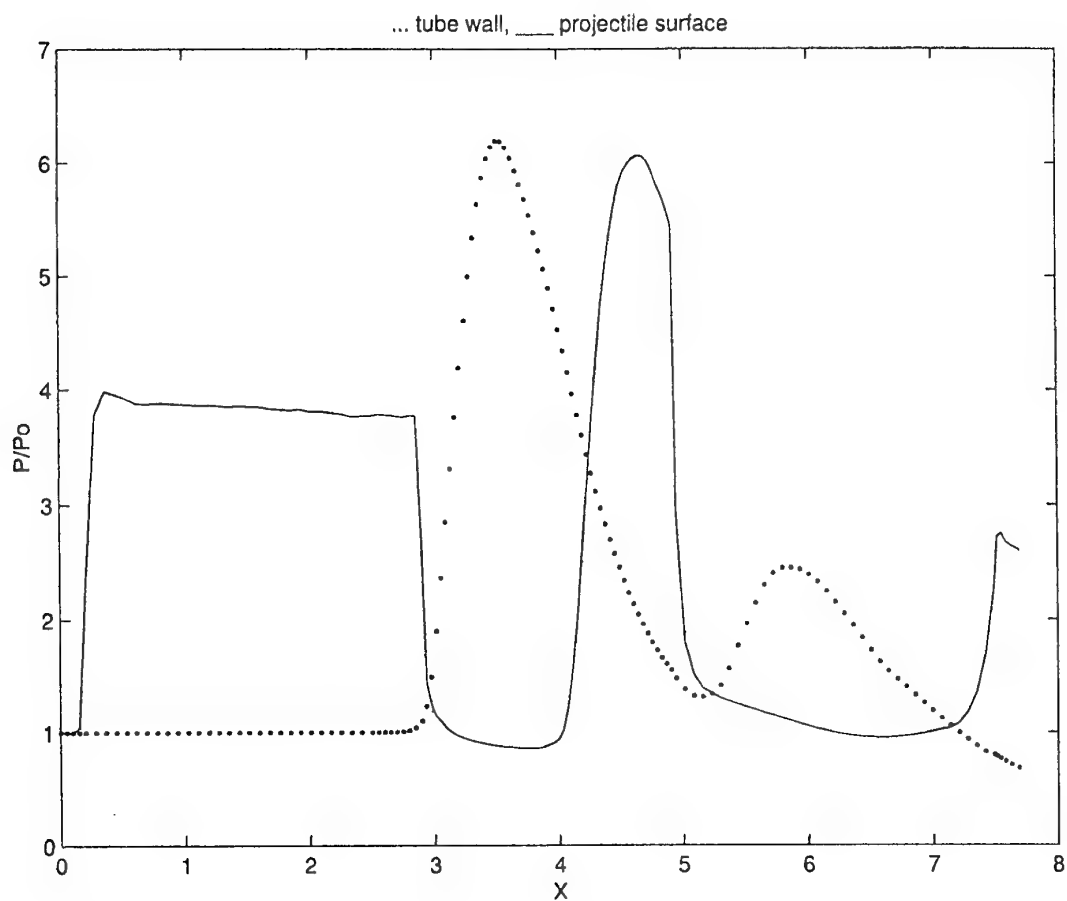


Figure 16: Pressure distribution along the tube wall and the projectile surface under the cold flow condition

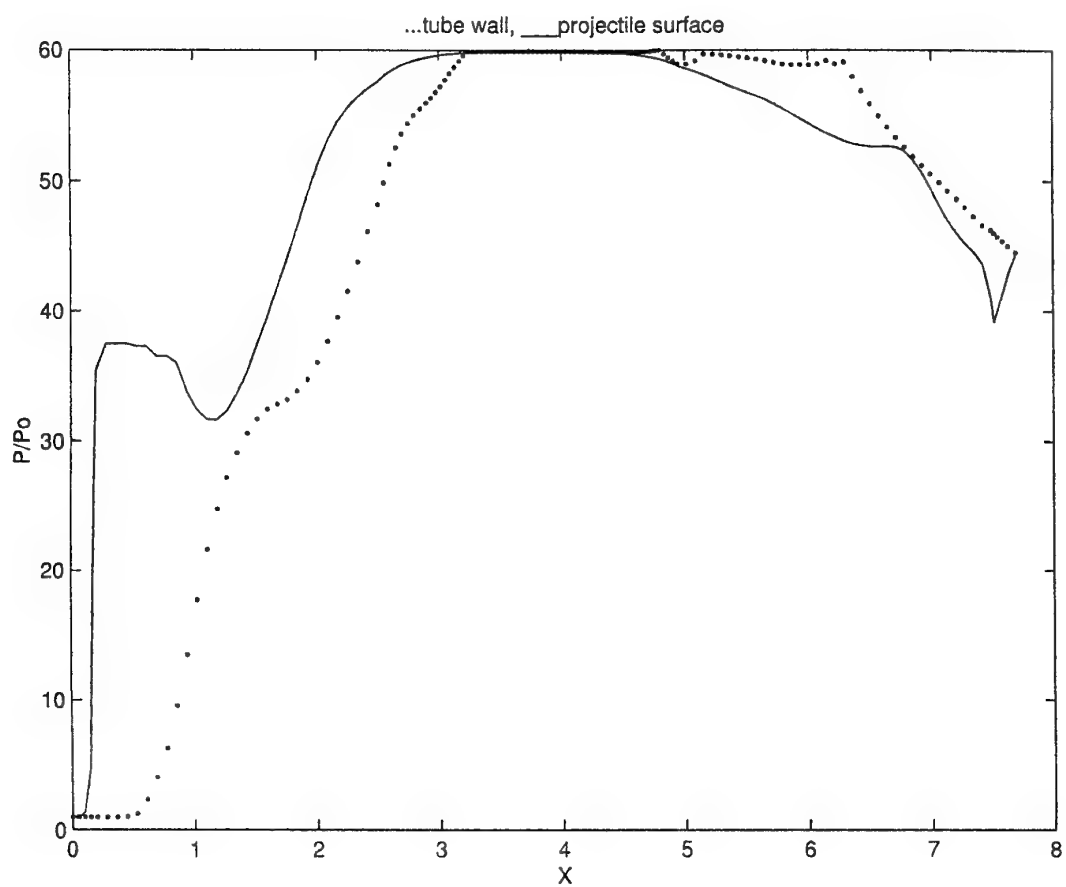


Figure 17: Pressure distribution with combustion

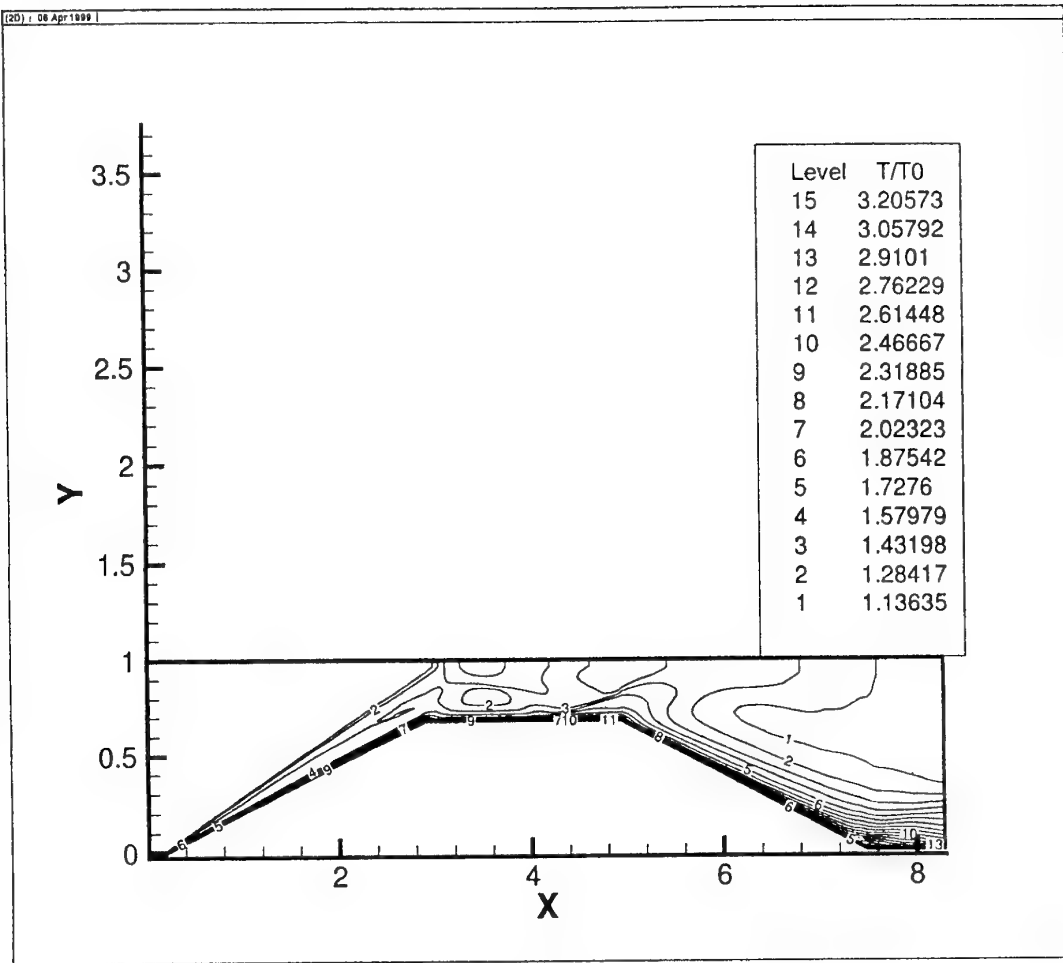


Figure 18: Temperature contours (cold flow)

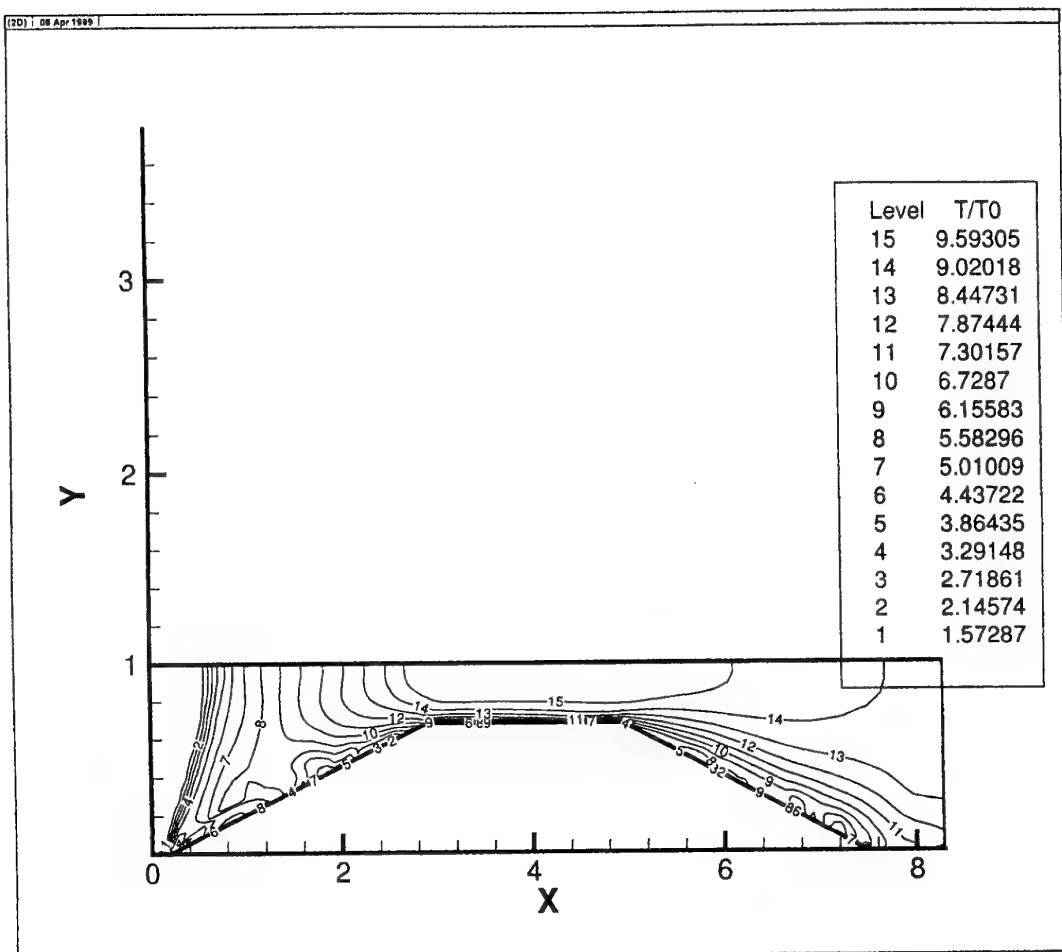


Figure 19: Temperature contours (with combustion)

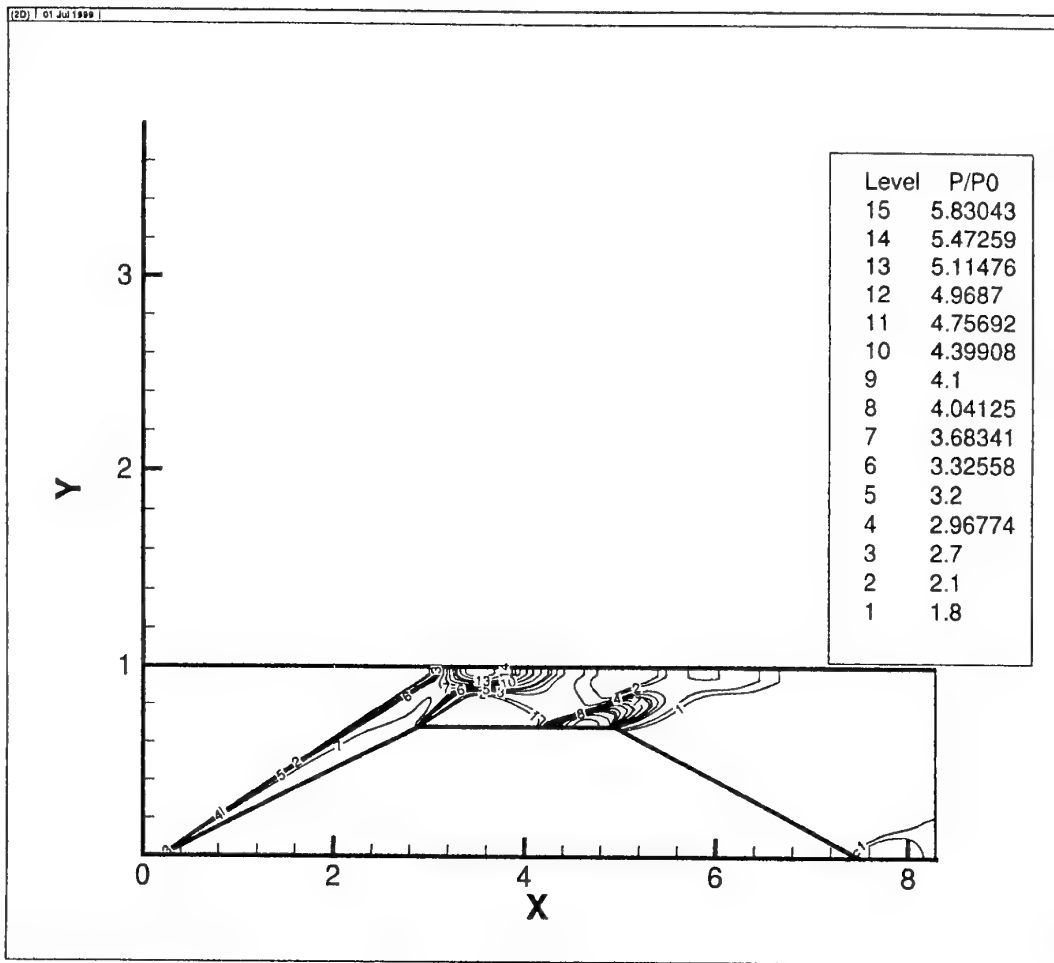


Figure 20: Pressure contours (cold flow)

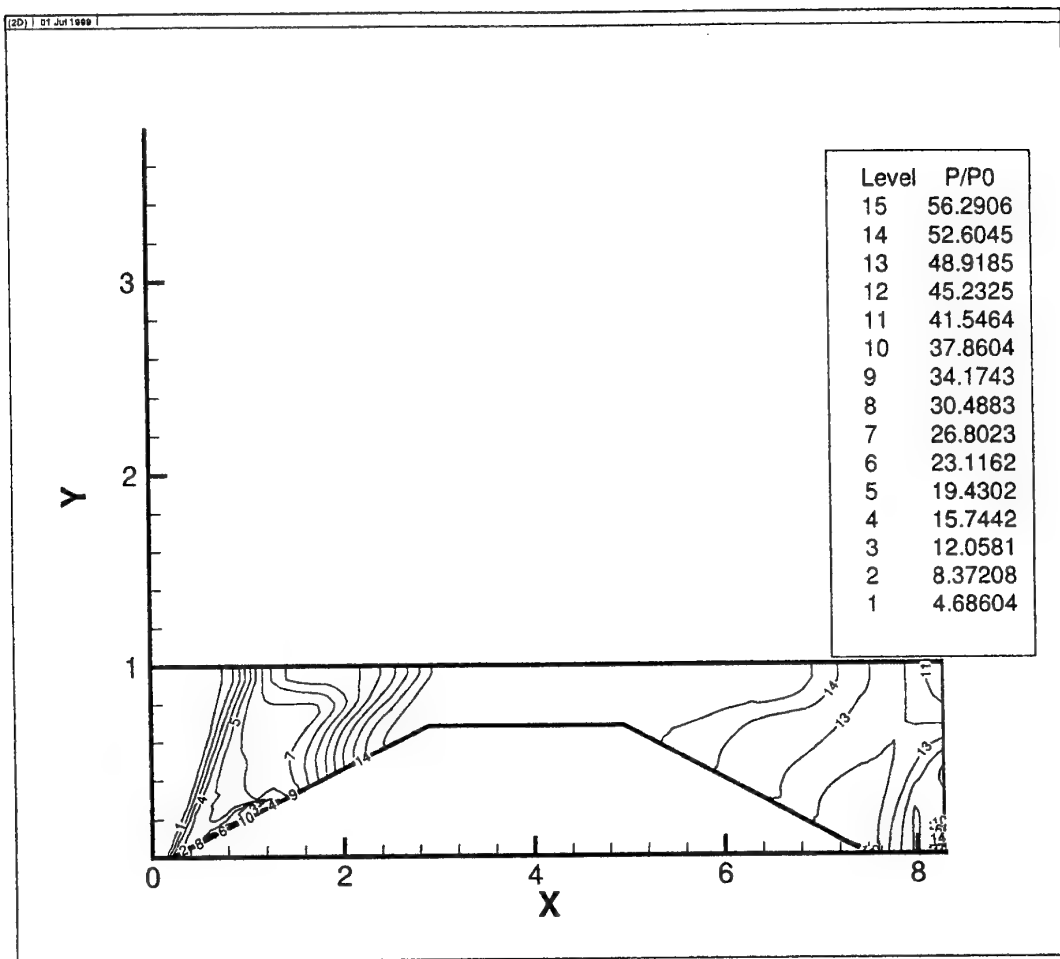
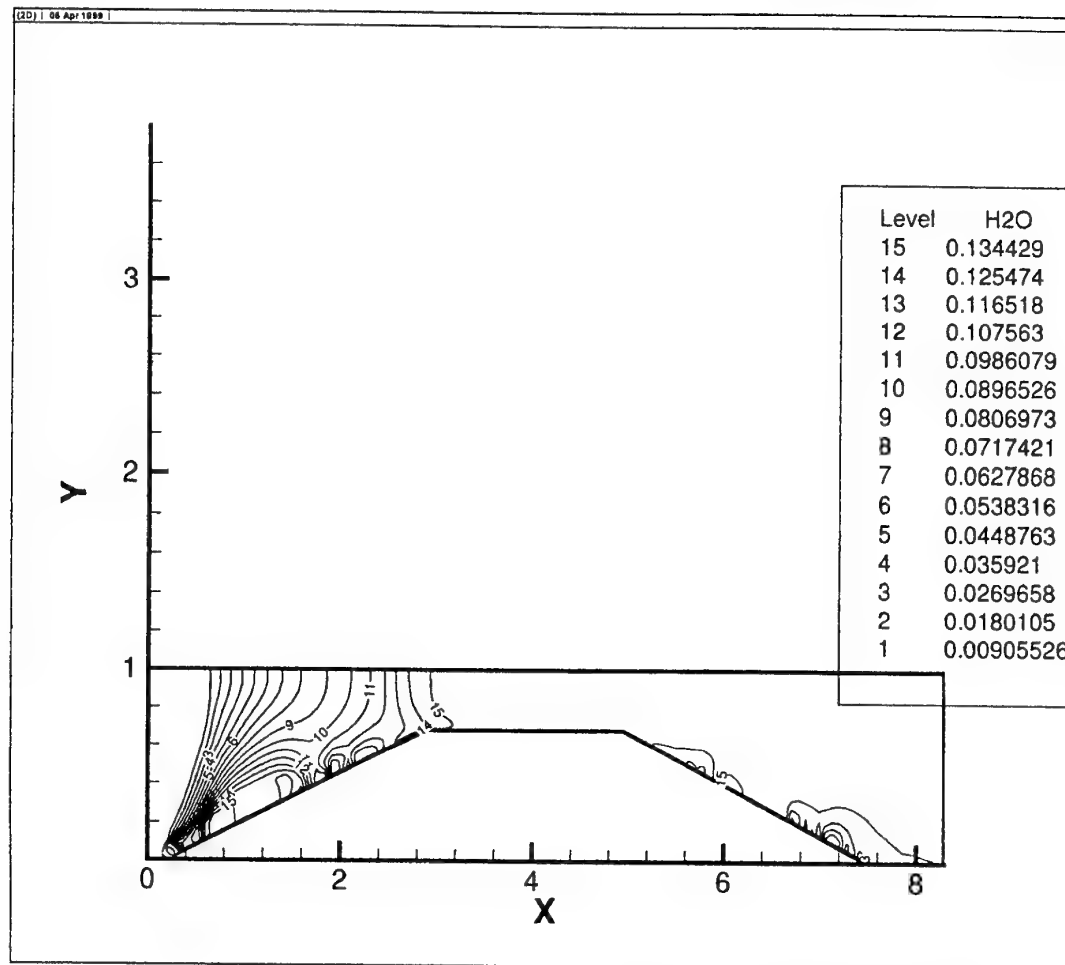
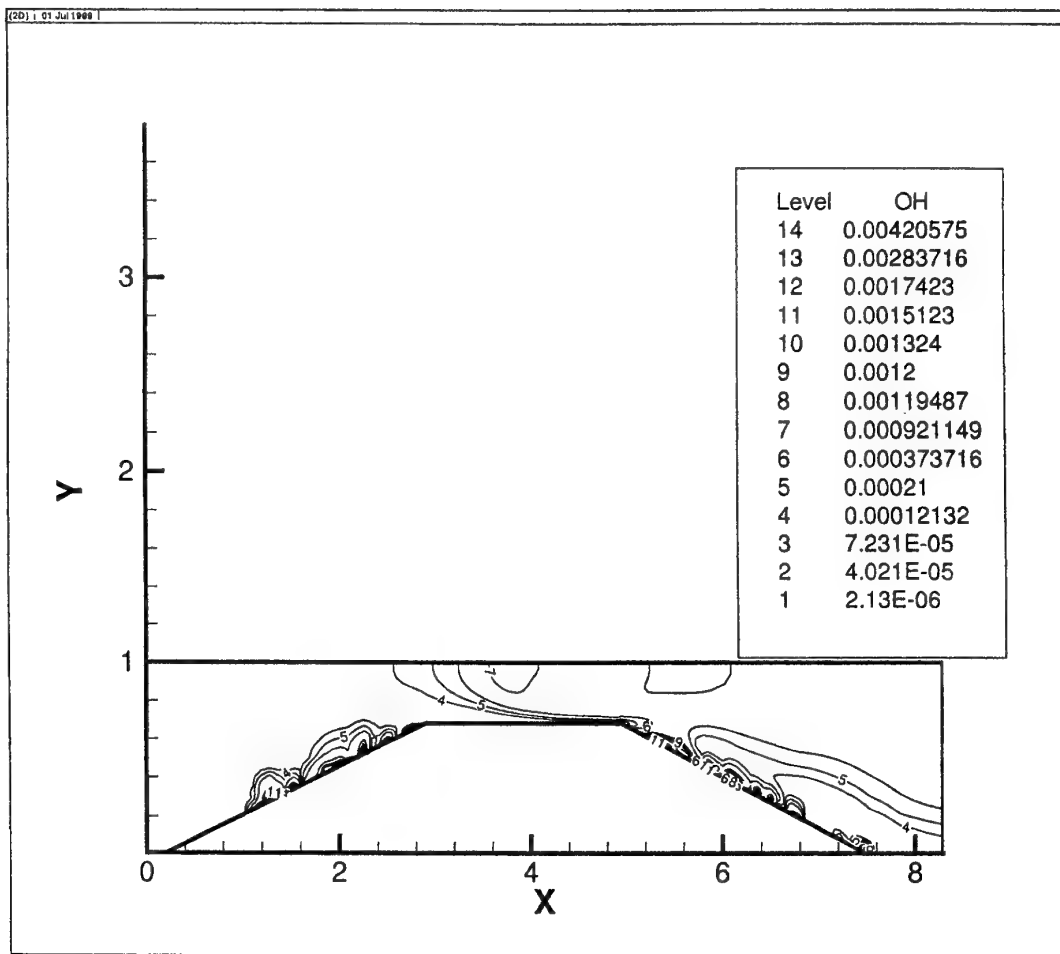


Figure 21: Pressure contours (with combustion)

Figure 22:  $H_2O$  mass fraction contours

Figure 23: *OH* mass fraction contours

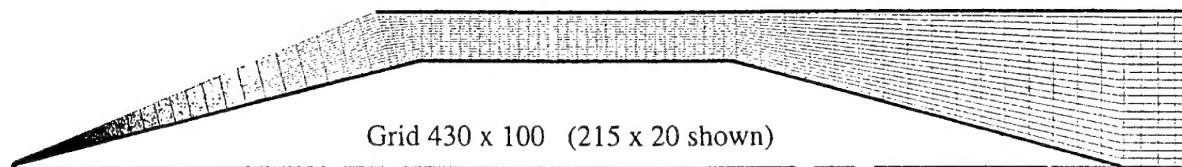


Fig. 24 Grid system used by Leblanc for the simulation. The grid points conform to the nose tip. Longitudinal grid points are more densely packed at the throat.

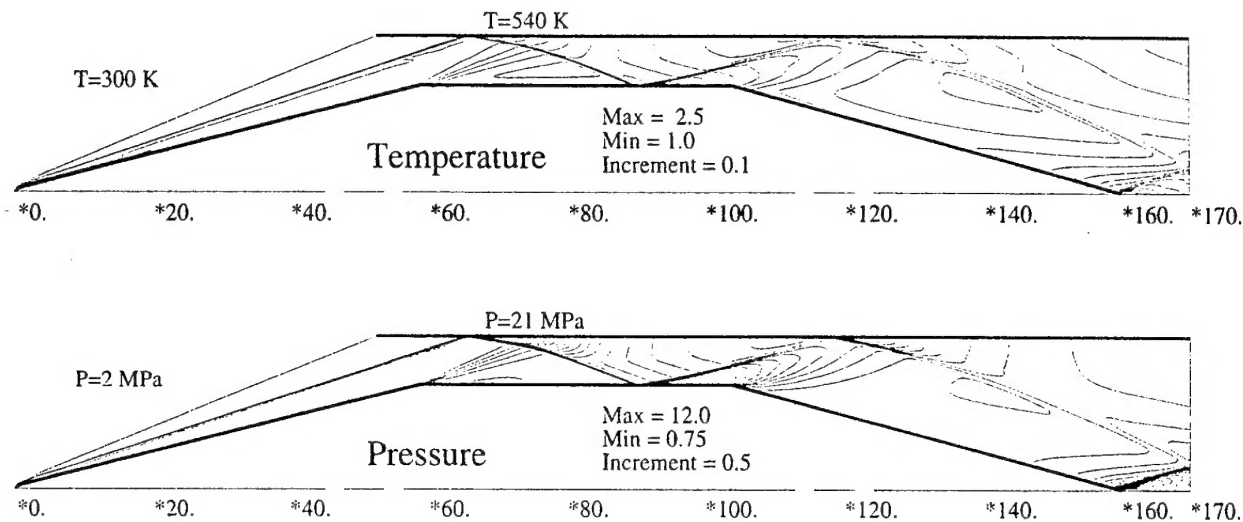


Fig. 25 Contour plots of the non-reactive simulation. Specific value above the throat is the peak pressure and temperature calculated at the wall. Maximum values exclude the stagnation value at the nose tip.

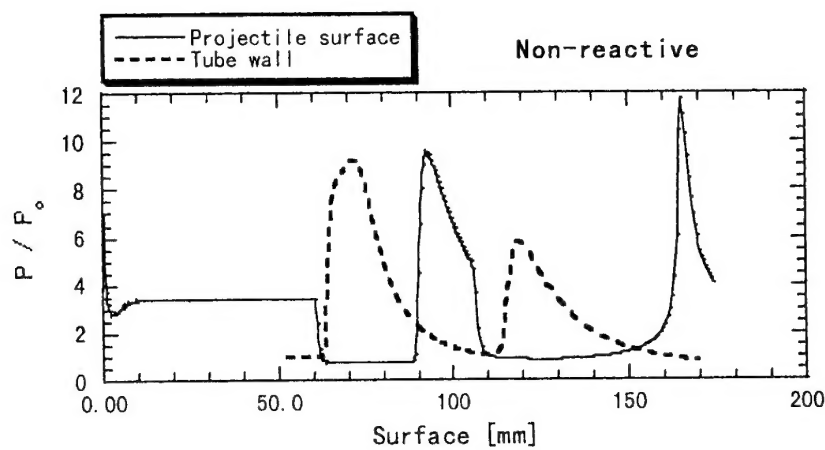


Fig. 26 Plot of pressure on projectile surface and tube wall for non-reactive simulation.

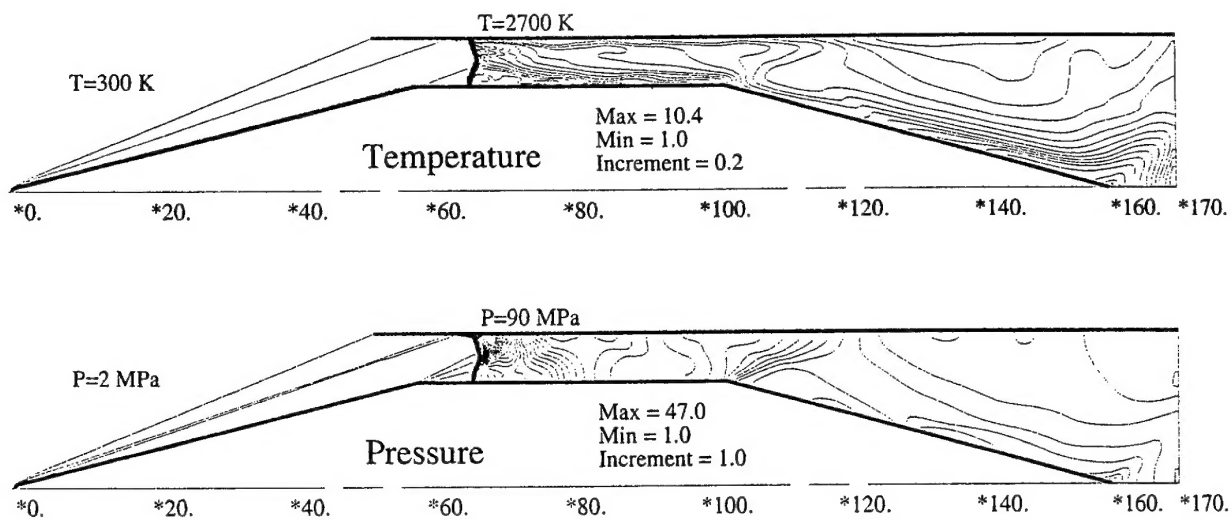


Fig. 27 Contour plots of the chemically reactive simulation. Specific value above the throat is the peak pressure and temperature calculated at the wall. Maximum values exclude the stagnation value at the nose tip.

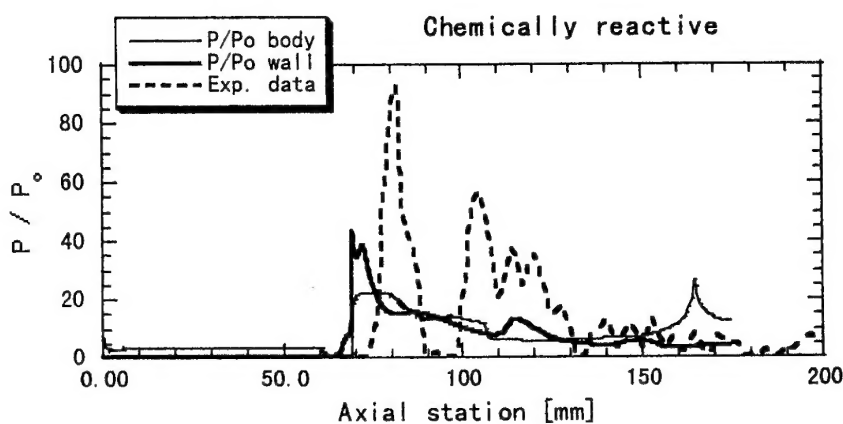


Fig. 28 Non-dimensional pressure on tube wall and projectile surface compared with experimental data of station M6 of Fig. 2

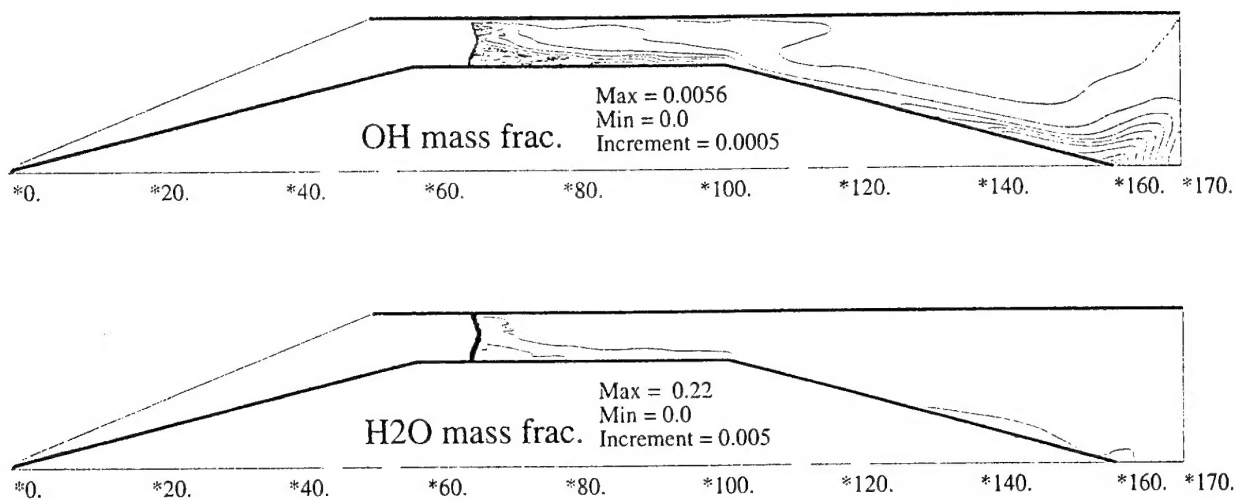


Fig. 29 Contour plots of the chemically reactive simulation. H<sub>2</sub>O mass fraction shows a very uniform level of water molecules behind the standing shock.

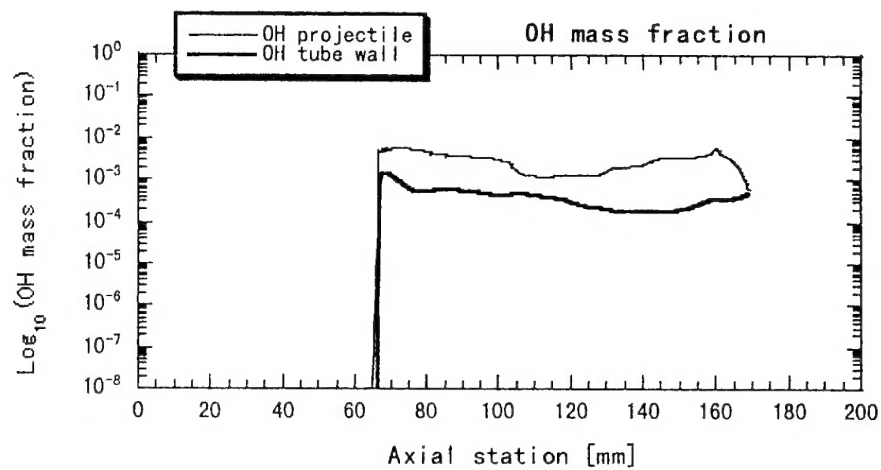


Fig. 30 Plot of OH mass fraction on the tube wall and projectile

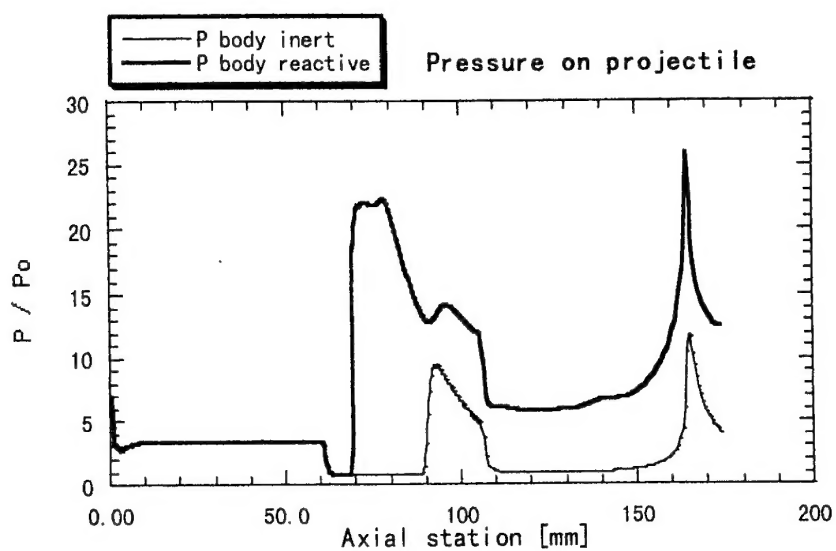


Fig. 31 Pressure on the projectile surface before and after chemical reaction takes place